On the opening angle of magnetized jets from neutron-star mergers

the case of GRB170817A

Nathanail, A.; Gill, R.; Porth, O.; Fromm, C.M.; Rezzolla, L.

DOI
10.1093/mnras/staa1454

Publication date
2020

Document Version
Final published version

Published in
Monthly Notices of the Royal Astronomical Society

Monthly Notices of the ROYAL ASTRONOMICAL SOCIETY

MNRAS **495**, 3780–3787 (2020)
Advance Access publication 2020 May 25

doi:10.1093/mnras/staa1454

On the opening angle of magnetized jets from neutron-star mergers: the case of GRB170817A

Antonios Nathanail,[1★] Ramandeep Gill,[2,3] Oliver Porth,[4] Christian M. Fromm[1,5] and Luciano Rezzolla[1,6]

[1] *Institut für Theoretische Physik, Goethe Universität Frankfurt, Max-von-Laue-Str.1, D-60438 Frankfurt am Main, Germany*
[2] *Department of Physics, The George Washington University, Washington, DC 20052, USA*
[3] *Department of Natural Sciences, The Open University of Israel, 1 University Road, P.O. Box 808, Raanana 4353701, Israel*
[4] *Astronomical Institute Anton Pannekoek, Universeit van Amsterdam, Science Park 904, NL-1098 XH, Amsterdam, The Netherlands*
[5] *Max-Planck-Institut für Radioastronomie, Auf dem Hügel 69, D-53121 Bonn, Germany*
[6] *School of Mathematics, Trinity College, Dublin 2, Ireland*

Accepted 2020 May 17. Received 2020 April 24; in original form 2020 March 10

ABSTRACT

The observations of GW170817/GRB170817A have confirmed that the coalescence of a neutron-star binary is the progenitor of a short gamma-ray burst (GRB). In the standard picture of a short GRB, a collimated highly relativistic outflow is launched after merger and it successfully breaks out from the surrounding ejected matter. Using initial conditions inspired from numerical-relativity binary neutron-star merger simulations, we have performed general-relativistic hydrodynamic (HD) and magnetohydrodynamic (MHD) simulations in which the jet is launched and propagates self-consistently. The complete set of simulations suggests that: (i) MHD jets have an intrinsic energy and velocity polar structure with a 'hollow core' subtending an angle $\theta_{\rm core} \approx 4^\circ$–$5^\circ$ and an opening angle of $\theta_{\rm jet} \gtrsim 10^\circ$; (ii) MHD jets eject significant amounts of matter and two orders of magnitude more than HD jets; (iii) the energy stratification in MHD jets naturally yields the power-law energy scaling $E(>\Gamma\beta) \propto (\Gamma\beta)^{-4.5}$; (iv) MHD jets provide fits to the afterglow data from GRB170817A that are comparatively better than those of the HD jets and without free parameters; and (v) finally, both of the best-fitting HD/MHD models suggest an observation angle $\theta_{\rm obs} \simeq 21^\circ$ for GRB170817A.

Key words: MHD – gamma-ray burst: general – stars: neutron.

1 INTRODUCTION

The first detection of gravitational waves (GWs) from a binary neutron-star (BNS) merger, GW170817 (The LIGO Scientific Collaboration & The Virgo Collaboration 2017), was marked by a coincident detection of a short gamma-ray burst (GRB), GRB170817A (Savchenko et al. 2017; Goldstein et al. 2017). This was followed by observations across the electromagnetic (EM) spectrum, with the detection of the (The LIGO Scientific Collaboration et al. 2017) quasi-thermal kilonova emission in ultraviolet, optical, and near-infrared followed by the delayed detection of the non-thermal afterglow emission in the X- ($t > 8.9$ d; Troja et al. 2017), optical, and radio ($t > 16.4$ d; Hallinan et al. 2017) bands.

The continuous brightening of the broadband afterglow flux, with its peculiar shallow rise ($F_\nu \propto t^{0.8}$) to the peak at $t_{\rm pk} \simeq 150$ d post-merger (Lyman et al. 2018; Margutti et al. 2018; Mooley et al. 2018a), was interpreted using two main models. The first one considered a 'structured outflow' (e.g, Gill & Granot 2018), namely, a polar-structured jet with a narrow relativistic core surrounded by low-energy wings (e.g. Troja et al. 2017, 2018; D'Avanzo et al. 2018; Margutti et al. 2018; Lazzati et al. 2018; Lamb & Kobayashi 2018; Pozanenko et al. 2018; Beniamini & Nakar 2019). The second model considered a 'cocoon', namely, a wide-angle outflow expanding quasi-spherically and with radial velocity stratification (e.g. Kasliwal et al. 2017; Gottlieb, Nakar & Piran 2018; Mooley et al. 2018a). The subsequent observation of apparent superluminal motion of the radio flux centroid (Mooley et al. 2018b), together with the compact size of the radio image (i.e. $\lesssim 2$ mas) (Ghirlanda et al. 2019), strongly favoured the structured jet model as dominating the afterglow emission near and post $t_{\rm pk}$ (Lamb, Mandel & Resmi 2018).

Numerical and semi-analytical models of hydrodynamic (HD) jets have been employed to explore the afterglow of GRB170817A and the models that best fit the afterglow data correspond to structured jets with angular size of the relativistic core of $\sim 3^\circ$–5° (Mooley et al. 2018b; Ghirlanda et al. 2019; Troja et al. 2019; Lamb et al. 2019; Beniamini et al. 2019).

★ E-mail: nathanail@th.physik.uni-frankfurt.de

Table 1. Properties of the various HD and MHD jets considered: luminosity of the HD jet (L), injection time of HD jet ($t_{\rm inj}$), initial Lorentz factor of the HD jet ($\Gamma_{\rm init}$), initial opening angle of the HD jet ($\theta_{\rm jet}$), toroidal and poloidal magnetic energies (E_{B_ϕ}, $E_{B_{\rm p}}$) and their ratio, maximum magnetization in the torus ($\sigma := B^2/4\pi\rho$), minimum plasma parameter in torus ($\beta := p/p_m$, where p and p_m are the fluid and magnetic pressures respectively), maximum density of the torus ($\rho_{\rm max}$) and dimensionless spin parameter of the BH ($a := J/M^2$), initial total mass ($M_{\rm tot} = M_{\rm tor} + M_{\rm ext}$, where $M_{\rm tor}$ is the initial torus mass, and $M_{\rm ext}$ is the mass surrounding the torus and which initially is bound; in all simulations $M_{\rm ext} = 0.02\,{\rm M_\odot}$), unbound ejected mass at the end of the simulation ($M_{\rm ej}$) and their ratio.

Model	L (erg s^{-1})	$t_{\rm inj}$ (s)	$\Gamma_{\rm init}$	$\theta_{\rm jet}$ (deg)	E_{B_ϕ} (erg) 10^{49}	$E_{B_{\rm p}}$ (erg) 10^{49}	$\frac{E_{B_{\rm p}}}{E_{B_\phi}}$	$\sigma_{\rm max}$	$\beta_{\rm min}$	$\rho_{\rm max}$ (g cm^{-3}) 10^{10}	a	$M_{\rm tot}$ (M$_\odot$)	$M_{\rm ej}$ (M$_\odot$)	$\frac{M_{\rm ej}}{M_{\rm tot}}$ (per cent)
`HD-tht.6`	10^{51}	0.1	10	6	–	–	–	–	–	1.5	0.9375	0.108	0.0001	0.12
`HD-tht.3`	10^{51}	0.1	10	3	–	–	–	–	–	1.5	0.9375	0.108	0.0001	0.13
`MHD-p2t.03`	–	–	–	–	5.0	1.6	0.3	0.065	0.13	1.5	0.9375	0.108	0.039	36.0
`MHD-p2t.02`	–	–	–	–	10	2.1	0.2	0.065	0.13	2.0	0.9375	0.144	0.053	37.1
`MHD-p2t.12`	–	–	–	–	1.2	1.5	1.2	0.036	0.13	1.5	0.9375	0.108	0.036	34.1

Most of the analysis for the outflow of GRB170817A has been done using semi-analytical models or relativistic HD simulations that launch a jet far from the merger site, with launching radius of 10^9 cm. These HD studies have been accompanied by much fewer investigations making use of magnetohydrodynamic (MHD) simulations to study the properties of such outflows (Kathirgamaraju, Barniol Duran & Giannios 2018; Bromberg et al. 2018; Geng et al. 2019), and in two cases, the jets were launched self-consistently via the accretion and rotation of the black hole (BH, Fernández et al. 2019; Kathirgamaraju et al. 2019). In addition to such self-consistent evolutions, Kathirgamaraju et al. 2019 were also the first to report afterglow light curves as derived from the MHD simulations.

We here report on a series of 2D general-relativistic MHD (GRMHD) simulations of jets that are self-consistently launched after a BNS merger when the merger remnant has collapsed to a BH. In addition, we also carry out simulations in general-relativistic HD – where the jet is artificially powered via the injection of energy near the BH – and use these simulations to compare and contrast the properties of the MHD and HD jets.

2 MHD VERSUS HD JETS

We employ BHAC to solve the GRMHD equations in a Kerr background space–time (Porth et al. 2017). In order to describe the ejected matter and the torus around the compact remnant that was produced after a BNS merger, we follow the setup introduced in Nathanail, Porth & Rezzolla (2019) and additional information on the numerical setup are reported in Appendix A. The properties of the models simulated study are listed in Table 1.

HD jets have been thoroughly studied in the context of short GRBs from BNS mergers (Nagakura et al. 2014; Murguia-Berthier et al. 2014, 2016; Duffell, Quataert & MacFadyen 2015; Lamb & Kobayashi 2017; Duffell et al. 2018; Hamidani, Kiuchi & Ioka 2020). The MHD jets in our simulations are launched self-consistently over the time-scale of the simulations, which ranges between $\sim$ 40 ms (for most cases) and $\sim$ 160 ms. Overall, the dynamics of the plasma can be briefly described as follows: starting from a non-self-gravitating torus with initial size $r_{\rm in} = 6M = 23.8$ km and $r_{\rm out} = 14.3M = 56.7$ km and containing a magnetic field of various topologies and strengths (cf. Table 1), the magnetorotational instability (MRI) develops, driving the accretion of matter and magnetic flux on to the BH. At the same time, the magnetic pressure in the torus expels the outer layers with an efficiency that depends strongly on the initial plasma β parameter in the torus. As the MRI saturates and accretion reaches a steady state, the funnel region above the BH is cleared up and an MHD jet is formed. This accretion process can then continue until either the torus is accreted and ejected, or when the BH has lost much of its reducible energy by spinning down (Nathanail, Strantzalis & Contopoulos 2016).

As the MHD jet breaks out from the ejecta that, in our setup, terminate at a radius of 1200 km, it enters in a region of low-density material where it does not encounter any matter pressure gradient that contributed to its collimation. As a result, the jet expands in the transversal direction while maintaining a high degree of collimation. More precisely, when the head of the jet reaches $\sim$ 1500 km, the opening angles at a distance of $\sim$ 500 km and $\sim$ 1500 km are $\theta_{\rm jet} \simeq 13^\circ$ and $\simeq 15^\circ$, respectively. By the time, the MHD jet reaches the outer boundary of the computational domain at $\sim$ 10 000 km, the opening angle is still very small and $\theta_{\rm jet} \simeq 13^\circ$. These values depend in detail on the initial conditions of the jet and on the properties of the ambient medium (Tchekhovskoy, McKinney & Narayan 2008), but do not vary significantly in the simulations we have considered.

Another robust feature in all our MHD models reported in Table 1, is an almost hollow core subtending an angle $\theta_{\rm core} \approx 4^\circ$–$5^\circ$, thus much smaller than the overall opening angle of the MHD jet, $\theta_{\rm jet} \gtrsim 10^\circ$; the latter is consistent with numerical-relativity simulations where the starting point for the launching of such a jet is reached (Rezzolla et al. 2011; Kiuchi et al. 2014; Dionysopoulou, Alic & Rezzolla 2015; Kawamura et al. 2016; Ruiz et al. 2016).[1] In Fig. 1, we show a comparison between an MHD and an HD jet, where both jets have passed through the torus and the ejected matter. The Lorentz factor, shown on the left-hand panel, clearly tends to unity in the inner core of the MHD jet. The appearance of a hollow cone in MHD jets has been pointed out previously in the literature (Komissarov et al. 2007; Tchekhovskoy et al. 2008; Lyubarsky 2009), but these were smaller than the one found here in our simulations inspired by BNS merger scenarios. It is important to remark that a hollow core appears in all MHD jet models simulated here, independently of the various initial conditions considered (see Appendix A for more details).

The structure and opening angle of the jet models presented in these studies depend strongly on the collimating agent. In the case of long GRBs, this agent is represented by the disc wind and the stellar layers that the jet has to bore. On the other hand, in the case of short GRBs produced from BNS mergers, once the jet breaks out from the matter ejected by the merger, it encounters the low-density

[1]While 'hollow core' is a standard denomination, the core of the jet does actually contain matter, but with very small Lorentz factor and energy.

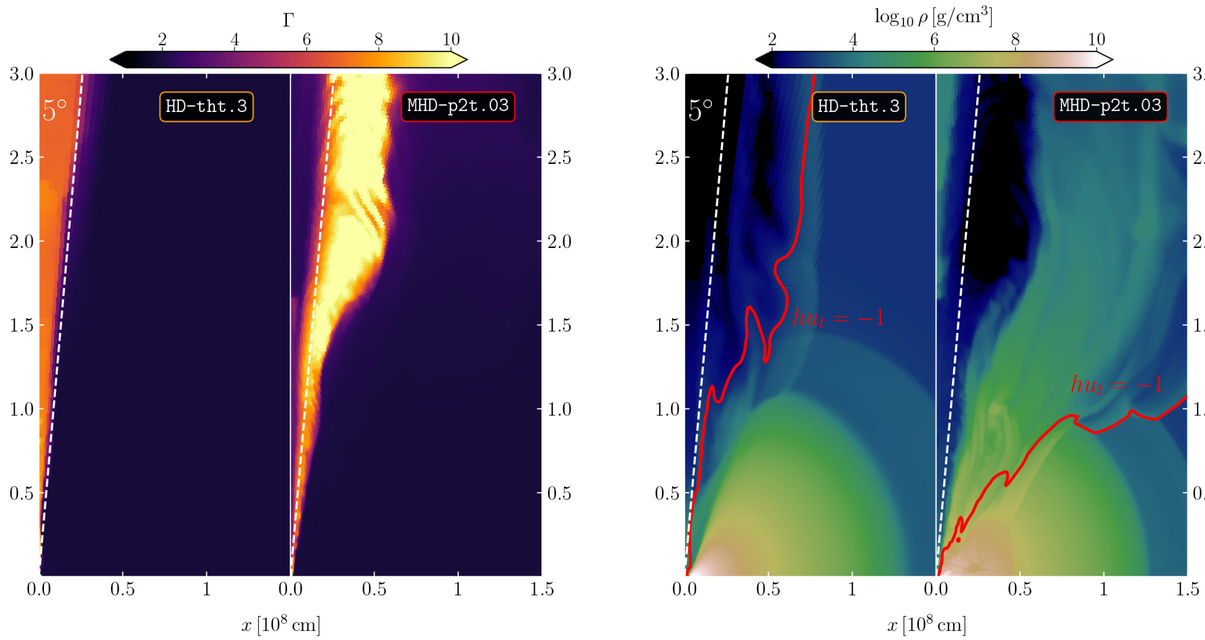

Figure 1. Lorentz factor (left-hand panel) and density (right-hand panel) distribution for two representative models: `MHD-p2t.03` (left-hand part of each plot) and `HD-tht.3` (right-hand part of each plot). The dashed white line indicates a cone with opening angle of 5°, highlighting the slow core of the MHD jet model. On the right-hand panel, the red solid lines denote the contour of $hu_t = -1$, so that matter above such line is gravitationally unbound; clearly the amount of ejected mass from the MHD jet is significantly larger than in the HD jet model.

interstellar medium (ISM), with number densities $n_{\rm ISM} \sim 10^{-3}$–10^{-1} cm^{-3}, so that no significant further collimation is expected after breakout.

Duffell et al. (2018) have shown that as an HD jet drills through merger ejecta, it does not deposit significant energy, and thus has limited impact on the amount of ejected mass and the appearance of a kilonova. This is in stark contrast with what happens for MHD jets, the magnetized torus produces winds, with velocities far below the relativistic jet but significant enough that a large fraction of the initial matter distribution becomes unbound. On the right-hand panel of Fig. 1, we show the distribution of the rest-mass density at time $t \sim 26$ ms, after the MHD and the HD jets have broken out from the merger ejecta. To quantify how much matter becomes unbound, we employ the Bernoulli criterion and assume a fluid element to be unbound if it has a Bernoulli constant $hu_t \leq -1$, where h is the specific enthalpy of the fluid (Rezzolla & Zanotti 2013). We then apply this criterion to measure the flux of unbound matter on a two sphere of 4000 km and report in last two columns of Table 1 the amount of ejected mass and the fraction of the ejected mass with respect to the initial mass of the torus. Note that in all cases considered the ejected mass is between a few per cent of the initial mass and up to a maximum of 37 per cent; furthermore, models with higher initial σ, have a larger fraction of unbound matter.

The angular structure of the HD and MHD jets can be better appreciated through the polar plots in Fig. 2, where we report the Lorentz factor and the energy, that is the volume integral up to the outer boundary of the *total* energy density, relative to the *unbound* material of three representative MHD jets and of the HD jet. The Lorentz factor (left-hand panel of Fig. 2) is measured on a two sphere with radius $r \sim 2000$ km, and is integrated over a time interval of $\tau_{\rm avg} \sim 4$ ms to capture both the variability and the steady features.

Each of the four quadrants refers to one of the models considered, that is `MHD-p2t.03`, `MHD-p2t.02`, `MHD-p2t.12`, and `HD-tht.6`, with a thick line indicating the time-averaged values and with the shaded areas showing the 1σ variance over the time interval $\tau_{\rm avg}$, that is the 68 per cent variation of the Lorentz factor at each angle. The right-hand panel of Fig. 2, on the other hand, shows the angular distribution of the energy for the four models, where the energy is integrated for every angle for *unbound* matter with $\Gamma > 1.2$; such a cut-off is introduced to avoid the inclusion of comparatively slow material.

In Fig. 3, we show instead the energy distribution above a certain value of $\Gamma\beta$, that is $E(>\Gamma\beta)$, as a function of $\Gamma\beta$, both for the HD jet and for the three representative MHD models. Since the energy E generically grows with $\Gamma\beta$, the quantity $E(>\Gamma\beta)$ helps capture the non-linear growth as a deviation from a constant value and to determine the cut-off at the highest energies. The energy is measured after the jet has broken out from the merger ejecta, that is $t = 10$ ms, and is reported at three different times with a separation of 5 ms in time. Note that the HD jet is less powerful and with an energy that has an almost linear dependence $\Gamma\beta$ but to $\Gamma\beta \simeq 6$–7, when it has a very sharp fall-off profile at moderate Lorentz factors. Therefore, in an HD jet, a most of the energy is concentrated in the fast-moving material.

On the other hand, all the MHD jets are up to two orders of magnitude more powerful and have a sublinear growth of energy with $\Gamma\beta$; at the same time, the cut-off is less abrupt and preceded by a clear power-law fall-off at high Lorentz factors, which can be approximated as $E(>\Gamma\beta) \propto (\Gamma\beta)^{-4.5}$. Hence, in the case of MHD jets, most of the energy is at $\Gamma\beta \sim 10$, but the energy distribution in the plasma can reach very large values. Note that a cut-off of $\Gamma \simeq 20$ is set to avoid to account for portions of the flow where the accuracy of the numerical solution is reduced because of the large Lorentz factors reached.

It is worth noting that the bulk of our MHD jets is moving relatively fast and overall faster than what observed in other simulations (Gottlieb et al. 2018) or analytical modellings (Mooley et al. 2018a; Gill & Granot 2018), where most of the energy is in

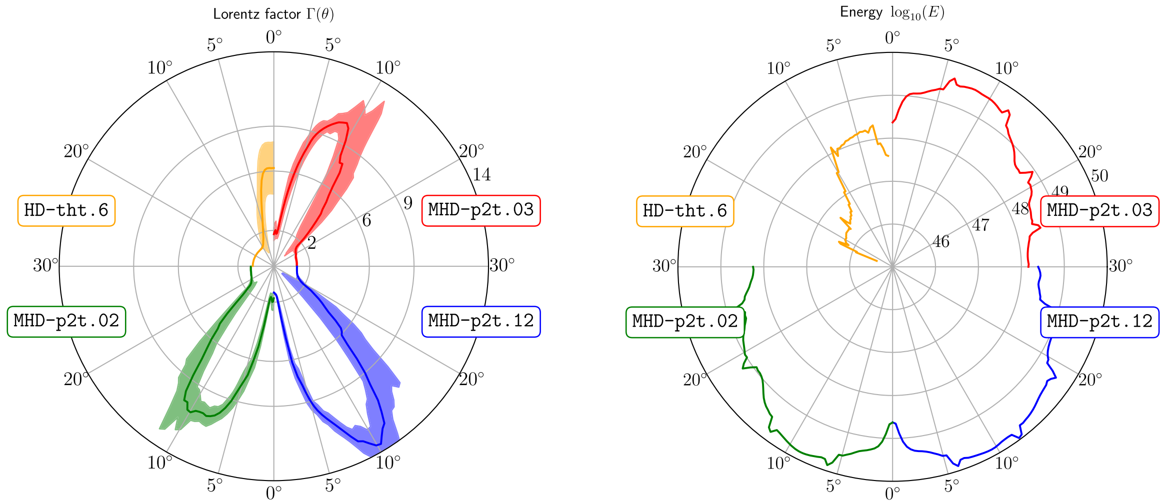

Figure 2. Left-hand panel: polar plot of the Lorentz factor for four representative outflows over a quadrant within a cone of 30°; and the thick lines show the time-averaged values, while the shaded region the 1σ variance. Right-hand panel: polar plot of the energy distribution for four representative models within a cone of 30°.

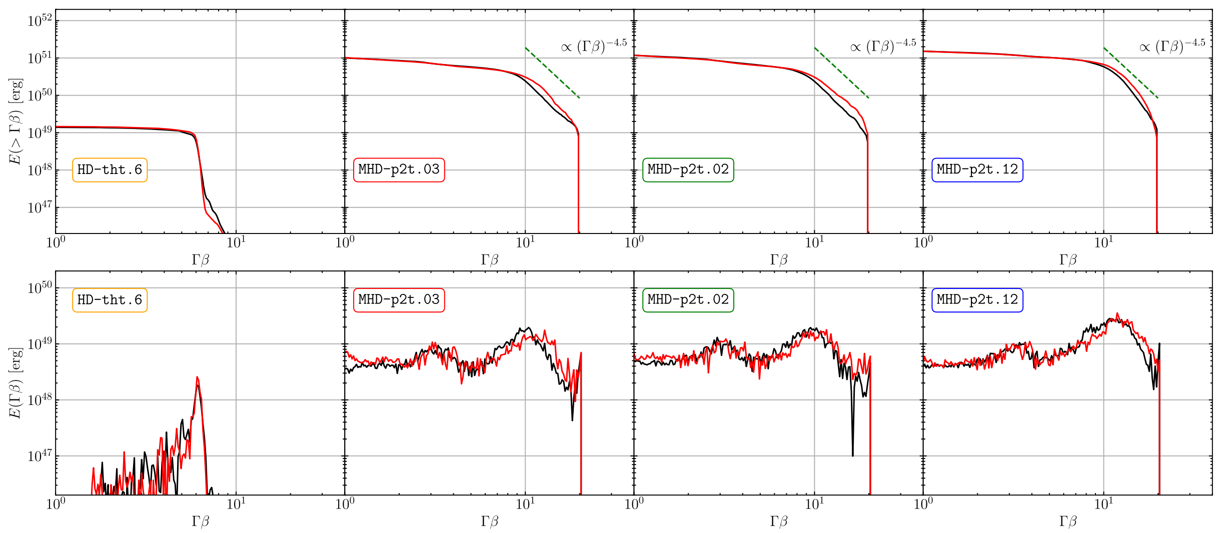

Figure 3. Energy distributions shown as either as $E = E(>\Gamma\beta)$ (top panels) or as $E = E(\Gamma\beta)$ (bottom panels) for the four representative models. The black and red solid lines represent the distribution at different times, $t = 15$ and 20 ms, respectively.

slow-moving material and the power-law behaviour $\Gamma\beta^{-(4-5)}$ is seen already for $\Gamma\beta \simeq 1$. As a final remark, we note that since our MHD jets are launched as a result of GRMHD accretion processes, their energetics cannot be steered from the initial conditions, but is the self-consistent result of the simulations.

3 AFTERGLOW EMISSION

The afterglow emission is expected to be dominated by synchrotron radiation from electrons at the forward shock propagating into the low-density ISM and that are accelerated into a power-law energy distribution of the type $n_e(\Gamma_e) \propto \Gamma_e^{-p}$, where n_e and Γ_e are the number density and Lorentz factors of the electrons, respectively; hereafter, we will assume $p = 2.16$, which is consistent with previous analysis for the afterglow of GRB170817A (Troja et al. 2019; Hajela et al. 2019). Following Sari, Piran & Narayan (1998), we model the emission that depends on the microphysical parameters ϵ_e and ϵ_B, which describe the fraction of the total internal energy behind the shock given to electrons and to the magnetic field, respectively. The afterglow light curves are computed following the angular distributions of the Lorentz factor and of the energy profile (cf. Fig. 2), together with the energy distribution in $\Gamma\beta$ (cf. Fig. 3). The angular structure is binned uniformly in 200 angles along the θ-direction, which yields the initial $\Gamma_0(\theta)$ and isotropic-equivalent energy $E_{\rm iso}(\theta)$ of the flow (see Granot, Piran & Sari 1999; Gill & Granot 2018, for details).

As representative examples of our fits, we make use of model `HD-tht.6` and model `MHD-p2t.03`. For the data, on the other hand, we employ the most recent afterglow data, that is $t \lesssim 743$ d after merger (see e.g. Hajela et al. 2019, for the latest observations in X-rays) consisting of X-ray emission at 5 keV and VLA radio observations at 3 and 6 GHz (Margutti et al. 2017, 2018; Alexander et al. 2017, 2018; Hallinan et al. 2017; Mooley et al. 2018a,c; Dobie et al. 2018; Troja et al. 2018, 2019; Hajela et al. 2019). The fit is performed with five free parameters, namely: the observer angle

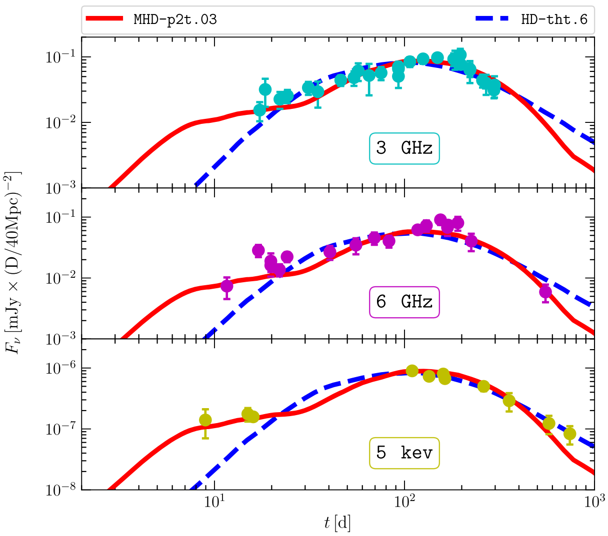

Figure 4. Broad-band observations of GRB170817A with the best-fitting light curves of models MHD-p2t.03 (red line; see the main text for the fitting parameters) and HD-tht.6 (dashed blue line; see the main text for the fitting parameters).

$\theta_{\rm obs}$, the energy of the burst E, the fraction of the total energy in the electrons ϵ_e, the fraction of the total energy in the magnetic field ϵ_B, and the circum-merger density, $n_{\rm ISM}$. Note that the parameter space is degenerate since the model parameters outnumber the available constraints from the data (see e.g. Gill et al. 2019). Also, note that even though we have not considered simulations of HD jet models having different jet energies, the results of the simulation performed here can be scaled trivially in terms of the jet luminosity and injection time, so that the energy of the jet is effectively a free parameter (Granot 2012). The best-fitting parameters are then found using a genetic algorithm to optimize the parameter selection and minimize the reduced χ^2_ν (Fromm et al. 2019), while the fitting procedure is applied simultaneously to the three different bands.

The afterglow light curves relative to the set of parameters providing the best fits for the two models MHD-p2t.03 and HD-tht.6, along with the observational data, are shown in Fig. 4 for a source at 40 Mpc, where the upper and middle panels correspond to radio observations at 3 and 6 GHz, while the lower panel to X-ray observations at 5 keV.

Overall, the MHD jet model MHD-p2t.03 yields a better fit to the data, with a reduced $\chi^2_\nu = 2.5$ and parameters $\theta_{\rm obs} = 21.5^\circ$, $E = 10^{50.85}$ erg, $\log_{10}(\epsilon_e) = -0.99$, $\log_{10}(\epsilon_B) = -4.4$, and $n_{\rm ISM} = 10^{-2.04}\,{\rm cm}^3$ (red line). It captures well the first data points in the afterglow, together with the peak and the fall-off (consistent with Takahashi & Ioka 2019). The HD jet model HD-tht.6, on the other hand, provides a less-good fit with reduced chi-squared are $\chi^2_\nu = 4.04$ and parameters $\theta_{\rm obs} = 21.4^\circ$, $E = 10^{51.01}$ erg, $\log_{10}(\epsilon_e) = -0.27$, $\log_{10}(\epsilon_B) = -2.8$, and $n_{\rm ISM} = 10^{-4.14}\,{\rm cm}^3$ (dashed blue line); however, it also yields a better match to the very late decay in the X-ray emission till 743 days after the merger (model HD-tht.3 has $\chi^2_\nu = 5.06$ and an HD jet with $\theta_{\rm jet} = 16^\circ$ has even larger reduced chi-squared). Interestingly, both of the best-fitting models suggest an observation angle $\theta_{\rm obs} \simeq 21^\circ$, which can then be taken as a robust feature of the emission of GRB170817A. Our estimates are thus consistent with those of Mooley et al. (2018b), Troja et al. (2019), and smaller than those coming from the semi-analytical and analytical models, which suggest instead $\theta_{\rm obs} \simeq 30^\circ$ (Hajela et al. 2019).

It is worth noting that when all the physical parameters – that is, E, ϵ_e, ϵ_B, and $n_{\rm ISM}$ – are kept the same, the HD/MHD light curves show a marked difference. Indeed, while both light curves have similar power-law rise and fall-offs, the evolution of peak times are considerably different, with the HD having a monotonic dependence of the peak times with the viewing angle, with peak times increasing as viewing angles become larger. The MHD light curves, instead, do not have a minimum peak time at the smallest viewing angle, but for $\theta_{\rm obs} \gtrsim \theta_{\rm core}$; the peak time then increases steeply as the viewing angle grows. This considerable difference between the two afterglow light curves disappears for larger angles, that is, when the jets are observed off-axis.

4 CONCLUSIONS

We have performed a number of general-relativistic HD and GRMHD simulations to model the launching of a jet after a BNS merger and contrast the dynamics and appearance of HD and MHD jets. Overall, we find that:

(i) MHD jets have an intrinsic energy and velocity structure in the polar direction characterized by a 'hollow core' subtending an angle $\theta_{\rm core} \approx 4^\circ$–$5^\circ$ and an opening angle of $\theta_{\rm jet\,>} \gtrsim 10^\circ$. HD jets, on the other hand, have a uniform energy and polar structure and much smaller opening angles of $\theta_{\rm jet} \sim 3^\circ$. (ii) MHD jets eject significant amounts of matter, amounting to $\lesssim 30$ per cent of the total mass of the system and about two orders of magnitude more than HD jets. (iii) The energy stratification in MHD jets naturally yields the power-law energy scaling $E(>\Gamma\beta) \propto (\Gamma\beta)^{-4.5}$ often introduced in analytical modelling. This feature is robust and does not require special tuning as is the case instead for HD jets. (iv) MHD jets provide fits to the afterglow data from GRB170817A in three different bands (3 GHz, 6 GHz, and 5 keV) that are not only very good but also comparatively better than those of the HD jets. While even better fits can be constructed with suitably constructed HD jets, the fit obtained with MHD jets is robust and without free parameters. (v) Both of the best-fitting HD/MHD models suggest an observation angle $\theta_{\rm obs} \simeq 21^\circ$ for GRB170817A.

While this is arguably the most comprehensive exploration of jet launching from BNS mergers, explore and contrasting for the first time HD and MHD jets, future work will have to include additional jet models, a closer comparison with other models proposed in the literature, and a step towards imaging in the radio band.

ACKNOWLEDGEMENTS

Support comes in part also from 'PHAROS', COST Action CA16214, and the LOEWE-Program in HIC for FAIR. The simulations were performed on the SuperMUC cluster at the LRZ in Garching, on the LOEWE cluster at the CSC in Frankfurt, and on the HazelHen cluster at the HLRS in Stuttgart. RG is supported by the ISF-NSFC joint research program (grant no. 3296/19).

REFERENCES

Abramowicz M., Jaroszynski M., Sikora M., 1978, A&A, 63, 221
Alexander K. D. et al., 2017, ApJ, 848, L21
Alexander K. D. et al., 2018, ApJ, 863, L18
Beniamini P., Nakar E., 2019, MNRAS, 482, 5430
Beniamini P., Petropoulou M., Barniol Duran R., Giannios D., 2019, MNRAS, 483, 840
Bovard L., Martin D., Guercilena F., Arcones A., Rezzolla L., Korobkin O., 2017, Phys. Rev. D, 96, 124005

Bromberg O., Tchekhovskoy A., Gottlieb O., Nakar E., Piran T., 2018, MNRAS, 475, 2971
D'Avanzo P. et al., 2018, A&A, 613, L1
Dietrich T., Ujevic M., Tichy W., Bernuzzi S., Brügmann B., 2017, Phys. Rev. D, 95, 024029
Dionysopoulou K., Alic D., Rezzolla L., 2015, Phys. Rev. D, 92, 084064
Dobie D. et al., 2018, ApJ, 858, L15
Duffell P. C., Quataert E., MacFadyen A. I., 2015, ApJ, 813, 64
Duffell P. C., Quataert E., Kasen D., Klion H., 2018, ApJ, 866, 3
Fernández R., Tchekhovskoy A., Quataert E., Foucart F., Kasen D., 2019, MNRAS, 482, 3373
Fishbone L. G., Moncrief V., 1976, ApJ, 207, 962
Foucart F., O'Connor E., Roberts L., Kidder L. E., Pfeiffer H. P., Scheel M. A., 2016, Phys. Rev. D, 94, 123016
Fromm C. M. et al., 2019, A&A, 629, A4
Fujibayashi S., Kiuchi K., Nishimura N., Sekiguchi Y., Shibata M., 2018, ApJ, 860, 64
Geng J.-J., Zhang B., Kölligan A., Kuiper R., Huang Y.-F., 2019, ApJ, 877, L40
Ghirlanda G. et al., 2019, Science, 363, 968
Gill R., Granot J., 2018, MNRAS, 478, 4128
Gill R., Granot J., De Colle F., Urrutia G., 2019, ApJ, 883, 15
Goldstein A. et al., 2017, ApJ, 848, L14
Gottlieb O., Nakar E., Piran T., 2018, MNRAS, 473, 576
Granot J., 2012, MNRAS, 421, 2610
Granot J., Piran T., Sari R., 1999, ApJ, 513, 679
Hajela A. et al., 2019, ApJ, 886, L17
Hallinan G. et al., 2017, Science, 358, 1579
Hamidani H., Kiuchi K., Ioka K., 2020, MNRAS, 491, 3192
Kasliwal M. M. et al., 2017, Science, 358, 1559
Kathirgamaraju A., Barniol Duran R., Giannios D., 2018, MNRAS, 473, L121
Kathirgamaraju A., Tchekhovskoy A., Giannios D., Barniol Duran R., 2019, MNRAS, 484, L98
Kawamura T., Giacomazzo B., Kastaun W., Ciolfi R., Endrizzi A., Baiotti L., Perna R., 2016, Phys. Rev. D, 94, 064012
Kiuchi K., Kyutoku K., Sekiguchi Y., Shibata M., Wada T., 2014, Phys. Rev. D, 90, 041502
Kiuchi K., Kyutoku K., Sekiguchi Y., Shibata M., 2018, Phys. Rev. D, 97, 124039
Komissarov S. S., Barkov M. V., Vlahakis N., Königl A., 2007, MNRAS, 380, 51
Lamb G. P. et al., 2019, ApJ, 870, L15
Lamb G. P., Kobayashi S., 2017, MNRAS, 472, 4953
Lamb G. P., Kobayashi S., 2018, MNRAS, 478, 733
Lamb G. P., Mandel I., Resmi L., 2018, MNRAS, 481, 2581
Lazzati D., Perna R., Morsony B. J., Lopez-Camara D., Cantiello M., Ciolfi R., Giacomazzo B., Workman J. C., 2018, Phys. Rev. Lett., 120, 241103
Lyman J. D. et al., 2018, Nat. Astron., 2, 751
Lyubarsky Y., 2009, ApJ, 698, 1570
Margutti R. et al., 2017, ApJ, 848, L20
Margutti R. et al., 2018, ApJ, 856, L18
Mooley K. P. et al., 2018a, Nature, 554, 207
Mooley K. P. et al., 2018b, Nature, 561, 355
Mooley K. P. et al., 2018c, ApJ, 868, L11
Murguia-Berthier A. et al., 2016, ApJ, 835, L34
Murguia-Berthier A., Montes G., Ramirez-Ruiz E., De Colle F., Lee W. H., 2014, ApJ, 788, L8
Nagakura H., Hotokezaka K., Sekiguchi Y., Shibata M., Ioka K., 2014, ApJ, 784, L28
Nathanail A., Strantzalis A., Contopoulos I., 2016, MNRAS, 455, 4479
Nathanail A., Porth O., Rezzolla L., 2019, ApJ, 870, L20
Porth O., Olivares H., Mizuno Y., Younsi Z., Rezzolla L., Moscibrodzka M., Falcke H., Kramer M., 2017, Comput. Astrophys. Cosmol., 4, 1
Pozanenko A. S. et al., 2018, ApJ, 852, L30
Radice D., Galeazzi F., Lippuner J., Roberts L. F., Ott C. D., Rezzolla L., 2016, MNRAS, 460, 3255
Rezzolla L., Zanotti O., 2013, Relativistic Hydrodynamics. Oxford University Press, Oxford, UK
Rezzolla L., Giacomazzo B., Baiotti L., Granot J., Kouveliotou C., Aloy M. A., 2011, ApJ, 732, L6
Ruiz M., Lang R. N., Paschalidis V., Shapiro S. L., 2016, ApJ, 824, L6
Sari R., Piran T., Narayan R., 1998, ApJ, 497, L17
Savchenko V. et al., 2017, ApJ, 848, L15
Sekiguchi Y., Kiuchi K., Kyutoku K., Shibata M., Taniguchi K., 2016, Phys. Rev. D, 93, 124046
Takahashi K., Ioka K., 2019, preprint (arXiv:1912.01871)
Tchekhovskoy A., McKinney J. C., Narayan R., 2008, MNRAS, 388, 551
The LIGO Scientific Collaboration et al., 2017, ApJ, 848, L12
The LIGO Scientific Collaboration, The Virgo Collaboration, 2017, Phys. Rev. Lett., 119, 161101
Troja E. et al., 2017, Nature, 551, 71
Troja E. et al., 2018, MNRAS, 478, L18
Troja E. et al., 2019, MNRAS, 489, 1919

APPENDIX A: NUMERICAL SETUP AND MHD MODELS

In this appendix, we provide details of the numerical setup of our simulations and further show results for an extensive selection of MHD models in order to check the robustness of the results. As anticipated, we use BHAC to solve the GRMHD equations in a Kerr background spacetime (Porth et al. 2017). To mimic the post-merger remnant in GW170817 and as initial condition for the launching of an MHD jet, we consider a non-self-gravitating torus (Fishbone & Moncrief 1976; Abramowicz, Jaroszynski & Sikora 1978) around a BH of mass $M = 2.7\,\mathrm{M}_{\odot}$ and various dimensionless spins (see Table 1). The radial extent of the initial matter distribution is set to be 1200 km, in order to account for the expansion of the torus, and also for the matter expelled during merger, which has reached such a distance. To accommodate such a large extension of matter, the numerical domain has always a radius of 10 000 km. Since we here focus on the production and launch of a jet, at the beginning of the simulation all matter is bound and set to have a zero velocity. However, we do measure the mass that becomes unbound as a result of the jet launching and compute its contribution to the kilonova at the end of the simulation. The simulations are performed in two spatial dimensions using a spherical polar coordinate system. The computational domain is resolved with either 1024×512 or 512×256 cells and with three refinement levels, thus yielding an effective resolution of 4092×2048 cells.

Over the past several years, a robust picture has been drawn on the distribution of the ejected matter after the merger. More specifically, BNS merger simulations indicate that the polar region is not entirely empty of matter (Sekiguchi et al. 2016; Foucart et al. 2016; Radice et al. 2016; Bovard et al. 2017; Dietrich et al. 2017; Fujibayashi et al. 2018). To reproduce such conditions, we fill the polar region with matter, having density that is 2.5 orders of magnitude less than the maximum density of the torus and a radial profile that scales like $r^{-1.5}$, with an exception for model `HD-tht.6`, where the matter in the polar region has 1 order of magnitude higher density, but has the same radial profile. In a typical BNS merger, the two stars have a mildly strong initial magnetic field, which is expected to be amplified during merger, either via the Kelvin–Helmholtz or the MRI, yielding a very magnetic energy $> 10^{50}$ erg, and with ratio between poloidal and the toroidal components that is ≈ 0.3 (Kiuchi et al. 2018). To reproduce the enhancement in the magnetic field after the merger, we initialize our simulations with a poloidal nested-loop magnetic field structure and a toroidal component that traces the fluid pressure; by tuning the strength of two components

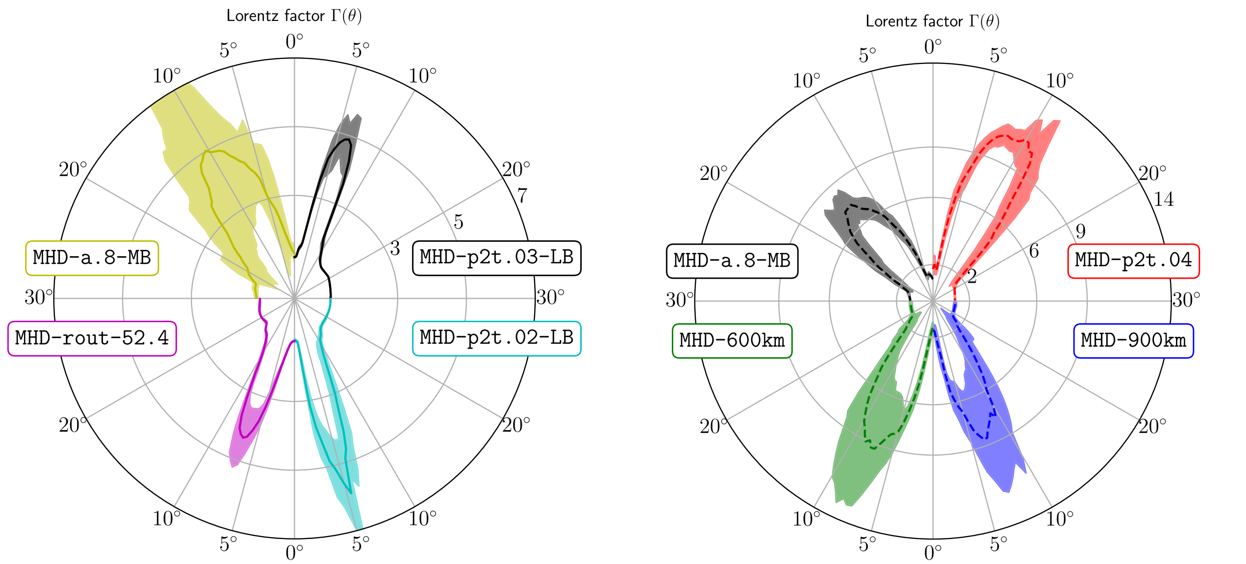

Figure A1. Polar plots of the Lorentz factor for eight outflows from Table A1 within a cone of 30°, the thick lines show the average values, while the shaded region the 1σ variance.

Table A1. Properties of the various HD and MHD jets considered: luminosity of the HD jet (L), injection time of HD jet ($t_{\rm inj}$), initial Lorentz factor of the HD jet ($\Gamma_{\rm init}$), initial opening angle of the HD jet ($\theta_{\rm jet}$), toroidal and poloidal magnetic energies (E_{B_ϕ}, $E_{B_{\rm p}}$) and their ratio, maximum magnetization in the torus ($\sigma := B^2/4\pi\rho$), minimum plasma parameter in torus ($\beta := p/p_m$, where p and p_m are the fluid and magnetic pressures respectively), maximum density of the torus ($\rho_{\rm max}$) and dimensionless spin parameter of the BH ($a := J/M^2$), initial total mass ($M_{\rm tot} = M_{\rm tor} + M_{\rm ext}$, where $M_{\rm tor}$ is the initial torus mass, and $M_{\rm ext}$ is the mass surrounding the torus and which initially is bound; in all simulations $M_{\rm ext} = 0.02\,{\rm M}_\odot$), unbound ejected mass at the end of the simulation ($M_{\rm ej}$) and their ratio. For all models the initial torus parameters are $r_{\rm in} = 23.8$ km, $r_{\rm out} = 56.8$ km, and the matter distribution has a radial extent till $r_{\rm ext} = 1200$ km, whereas model `MHD-rout-52.4` has $r_{\rm out} = 52.4$ km, model `MHD-600km` has $r_{\rm ext} = 600$ km and `MHD-900km` has $r_{\rm ext} = 900$ km. Note that models ending with MB and LB refer to matter with a medium and low magnetic-field strength, respectively, while all the other quantities are held the same.

Model	L (erg s^{-1})	$t_{\rm inj}$ (s)	$\Gamma_{\rm init}$	$\theta_{\rm jet}$ (deg)	E_{B_ϕ} (erg) 10^{49}	$E_{B_{\rm p}}$ (erg) 10^{49}	$\frac{E_{B_{\rm p}}}{E_{B_\phi}}$	$\sigma_{\rm max}$	$\beta_{\rm min}$	$\rho_{\rm max}$ (g cm^{-3}) 10^{10}	a	$M_{\rm tot}$ (M$_\odot$)	$M_{\rm ej}$ (M$_\odot$)	$\frac{M_{\rm ej}}{M_{\rm tot}}$ (per cent)
HD-tht.6	10^{51}	0.1	10	6	–	–	–	–	–	1.5	0.9375	0.108	0.0001	0.12
HD-tht.3	10^{51}	0.1	10	3	–	–	–	–	–	1.5	0.9375	0.108	0.0001	0.13
HD-tht.16	10^{51}	0.1	10	16	–	–	–	–	–	1.5	0.9375	0.108	0.0001	0.17
MHD-p2t.03	–	–	–	–	5.0	1.6	0.3	0.065	0.13	1.5	0.9375	0.108	0.039	36.0
MHD-p2t.03-LB	–	–	–	–	0.36	0.28	0.3	0.0026	3.20	2.0	0.9375	0.144	0.021	1.45
MHD-p2t.02	–	–	–	–	10	2.1	0.2	0.065	0.13	2.0	0.9375	0.144	0.053	37.1
MHD-p2t.02-LB	–	–	–	–	0.4	0.084	0.2	0.002	3.25	2.0	0.9375	0.144	0.002	1.60
MHD-p2t.12	–	–	–	–	1.2	1.5	1.2	0.036	0.13	1.5	0.9375	0.108	0.036	34.1
MHD-p2t.04	–	–	–	–	4.1	1.6	0.4	0.065	0.13	1.5	0.9375	0.108	0.033	31.2
MHD-a.8-LB	–	–	–	–	0.19	0.115	0.6	0.0024	3.30	3.0	0.8	0.118	0.0034	2.10
MHD-a.8-MB	–	–	–	–	1.7	1.05	0.6	0.02	0.36	3.0	0.8	0.118	0.014	12.0
MHD-a.8	–	–	–	–	3.9	2.4	0.6	0.06	0.13	2.5	0.8	0.098	0.029	29.8
MHD-rout-52.4	–	–	–	–	1.0	0.195	0.2	0.0016	4.10	10	0.9375	0.121	0.018	15.6
MHD-600km	–	–	–	–	1.7	0.54	0.3	0.016	0.52	2.0	0.9375	0.127	0.0077	6.23
MHD-900km	–	–	–	–	1.3	0.4	0.3	0.016	0.52	1.5	0.9375	0.106	0.004	3.94

it is then possible to obtain the desired ratio in the corresponding magnetic energies.

To explore a space of parameters that is as wide as reasonably possible, we vary the initial magnetic field, the ratio of the poloidal-to-toroidal magnetic-field energy, the spin of the BH, as well as the size and morphology of the torus (which is ultimately dictated by the spin of the BH). The details of all the models used are listed in Table A1. For illustrative purposes, we report in Fig. A1 the angular structure of eight outflows from Table A1, showing the Lorentz factor within an angle of $0 \leq \theta \leq 30°$. Similar to Fig. 2, the Lorentz factor (thick line) is measured in slices of constant radius , that is $r \sim 2000$ km, and integrated over a time interval of $\tau_{\rm avg} \sim 2$ ms, the shaded areas show the 1σ variance over the time interval $\tau_{\rm avg}$, that is the 68 per cent variation of the Lorentz factor at each angle. From the two polar plots it is evident that the presence of a hollow core with an opening of ≈4°–5° is robust in all of the MHD models considered in our study.

In the case of MHD jet models, the overall jet energy is proportional to the initial magnetic energy, whereas the Lorentz factor and opening angle turn out to be very similar in all MHD models. On the other hand, the jet energy, Lorentz factor, and opening angle for the HD models depend on the initial conditions chosen for the initial jet injection. Following the results in literature for GRB170817A and the modelling of its afterglow with HD models (which favour an opening angle of 3°–5°), we have chosen similar parameters for the initial conditions of the HD jet model. Furthermore, we have also considered an HD jet model with an opening angle of 16° (model `HD-tht.16` in Table A1). Because the overall jet energy depends trivially on the product of the duration of jet injection and of the jet power, we have used global scaling relations to obtain afterglow light curves for different jet energies.

This paper has been typeset from a TEX/LATEX file prepared by the author.